Journal of Biomedical Optics

BiomedicalOptics.SPIEDigitalLibrary.org

Optical coherence tomography with a 2.8-mm beam diameter and sensorless defocus and astigmatism correction

Maddipatla Reddikumar
Ayano Tanabe
Nobuyuki Hashimoto
Barry Cense

SPIE.

Maddipatla Reddikumar, Ayano Tanabe, Nobuyuki Hashimoto, Barry Cense, "Optical coherence tomography with a 2.8-mm beam diameter and sensorless defocus and astigmatism correction," *J. Biomed. Opt.* **22**(2), 026005 (2017), doi: 10.1117/1.JBO.22.2.026005.

Optical coherence tomography with a 2.8-mm beam diameter and sensorless defocus and astigmatism correction

Maddipatla Reddikumar,[a] Ayano Tanabe,[b] Nobuyuki Hashimoto,[b] and Barry Cense[a,*]
[a]Utsunomiya University, Center for Optical Research and Education, Utsunomiya, Tochigi, Japan
[b]Citizen Holding, Development Department, Tokorozawa, Saitama, Japan

Abstract. An optical coherence tomography (OCT) system with a 2.8-mm beam diameter is presented. Sensorless defocus correction can be performed with a Badal optometer and astigmatism correction with a liquid crystal device. OCT B-scans were used in an image-based optimization algorithm for aberration correction. Defocus can be corrected from −4.3 D to +4.3 D and vertical and oblique astigmatism from −2.5 D to +2.5 D. A contrast gain of 6.9 times was measured after aberration correction. In comparison with a 1.3-mm beam diameter OCT system, this concept achieved a 3.7-dB gain in dynamic range on a model retina. Both systems were used to image the retina of a human subject. As the correction of the liquid crystal device can take more than 60 s, the subject's spectacle prescription was adopted instead. This resulted in a 2.5 times smaller speckle size compared with the standard OCT system. The liquid crystal device for astigmatism correction does not need a high-voltage amplifier and can be operated at 5 V. The correction device is small (9 mm × 30 mm × 38 mm) and can easily be implemented in existing designs for OCT. [DOI: 10.1117/1.JBO.22.2.026005]

Keywords: optical coherence tomography; retinal imaging; adaptive optics; liquid crystal wavefront corrector; sensorless adaptive optics.

Paper 160671RR received Sep. 29, 2016; accepted for publication Jan. 23, 2017; published online Feb. 14, 2017.

1 Introduction

Optical coherence tomography (OCT) is a noninvasive, high-resolution optical imaging technique that is based on low coherence interferometry, and it is highly useful for generating cross-sectional images of turbid media. The first generation of OCT was in the time domain,[1] with depth scan rates up to about 1 kHz, making it difficult to perform *in vivo* imaging of biological samples such as the human retina without motion artifacts. The introduction of Fourier-domain optical coherence tomography (FD-OCT) has improved the imaging speed and sensitivity over time-domain optical coherence tomography (TD-OCT).[2,3] While the first spectral-domain OCT systems operated at depth scan rates of around 25 kHz, current systems can operate at speeds of 70 kHz or higher. High acquisition rates come with one penalty: the shorter acquisition time per depth scan causes a drop in sensitivity. To maintain image quality, one option is to increase the power that is incident on the sample. The ANSI safety rules for safe use of lasers limit the amount of light that can be sent into the eye.[4] Another option to improve image quality is to increase the photon collection efficiency of the sample arm. This can be achieved by using a larger beam size than the ∼1.2-mm beam diameter that is used in the sample arm of standard OCT instruments. Merits of a larger beam size are a decreased speckle size and improved lateral resolution, which is limited by the diffraction limit set by the beam size, the focal length of the eye, and the wavelength of the light. While OCT permits independent control of its lateral and axial resolutions, an increased numerical aperture limits the confocal depth of the system, which affects the image quality at depths above and below the beam waist. Furthermore, with increasing beam diameter, the aberrations induced by the eye increase as well.[5] To obtain these advantages and minimize the disadvantages caused by a large beam diameter, aberration correction is essential.

Adaptive optics (AO) is used in the field of astronomical optics to correct aberrations induced by atmospheric turbulence. Similar technology can be used for retinal imaging to achieve a diffraction-limited spot size.[6] OCT systems with a large beam diameter (∼6 mm) use an AO module, consisting of a Shack–Hartmann (SH) wavefront sensor for aberration sensing and a deformable mirror (DM) to generate the conjugate wavefront.[7] Unfortunately, these conventional AO-OCT systems tend to be complex, bulky, and cost-ineffective for use in a clinic.[8] Moreover, while a high lateral resolution of ∼3 μm is achieved over an isoplanatic patch (the area where the lateral resolution is diffraction limited)[9] of 1.5 deg or 450 μm,[10] in a clinical setting the field of view tends to be much larger, up to 30 deg by 30 deg.[8] While the small spot size and speckle size help to resolve small features, the Rayleigh length tends to be fairly small, only covering about half of the depth of the retina.[11]

Lower order aberration correction with cheap AO modules is of commercial interest. Recently, Verstraete et al.[12] demonstrated the correction of defocus and astigmatism with a liquid defocus lens and rotational cylindrical lenses, respectively. An SH wavefront sensor was combined with feedforward operation.

*Address all correspondence to: Barry Cense, E-mail: bcense@cc.utsunomiya-u.ac.jp

The omission of an SH sensor could further reduce costs in such a system. AO systems based on wavefront sensorless image optimization are popular in the fields of microscopy[13,14] and ophthalmoscopy.[15,16] Several groups have reported on wavefront sensorless AO-OCT systems with a DM and algorithm-based correction.[17–20] The algorithms were based on maximization of a merit function, providing images with high quality at the diffraction limit. To further reduce the cost and complexity of DM-based sensorless AO-OCT systems, alternative correction modules have been studied.[21,22] Recently, Bonora et al.[21] reported on a multiactuator lens for aberration correction up to the fourth Zernike order. The multiactuator lens requires a 16-channel high-voltage driver (±125 V). The lens was tested in an OCT system for imaging of mice retina, *in vivo*.[21] Due to the limited defocus correction ability of the multiactuator lens, a second correction module, a variable focal length, was used specifically for defocus correction.[22] The 4.8-mm-wide aperture of the system was corrected with five Zernike modes on human subjects.[22]

In wavefront-sensors-less AO-OCT, a sequential/coordinate search with a hill climbing algorithm,[17–19,21,22] annealing algorithm,[23] NEWUOA algorithm,[24] and data-based online nonlinear extremum-seeker (DONE) algorithm[25] have been implemented.

In this paper, we report on a system with a 2.8-mm beam diameter and image-based optimization and a low-cost AO module. The relationship between the pupil diameter and the required correction of aberration orders in terms of Zernike modes has been explained by Thibos et al.[5] For conventional OCT with a beam diameter of ~1.2 mm, only defocus needs to be corrected. At larger beam diameters, the number of Zernike modes that need to be corrected increases. A conventional AO-OCT system with a 6-mm beam diameter requires the correction of at least five-orders of Zernike modes. Following Thibos et al., the present system with a 2.8-mm diameter beam size requires the correction of at least two orders of Zernike modes: defocus, vertical astigmatism, and oblique astigmatism. Comparing standard OCT systems with a 1.2-mm beam and our approach, the advantages with 2.8-mm beam diameter are a reduction in speckle size of 2.3 times and an increase in lateral resolution of 2.3 times. The acceptance angle will be higher than in conventional OCT systems, which improves the collection efficiency. The practical imaging depth with a 6.0-mm beam-diameter AO-OCT system is less than half of the retina, while a 2.8-mm beam-diameter beam system should provide a practical imaging depth that is sufficiently long to cover the full retina.[8,11] The Rayleigh length (calculated with a 22.3-mm human eye focal length[26] and a 1.36 refractive index)[27] for the 1.2-mm beam diameter system is 269.5 μm; for a 6-mm beam diameter system, it is only 10.8 μm. A system with a 2.8-mm beam diameter has a 49.7-μm Rayleigh length. Using a model eye in Zemax,[8] the isoplanatic patch for the 1.2-mm beam diameter system is estimated at 30 deg × 30 deg for a 6.0-mm AO-OCT system it is 1.5 deg × 1.5 deg[9], whereas a system with a 2.8-mm aperture provides a 10 deg × 10 deg isoplanatic patch size. These numbers are compared in Table 1.

From Table 1 it can be concluded that the proposed OCT system fills a gap between conventional OCT systems with a 1.2-mm beam and conventional AO-OCT system with a 6-mm beam diameter. Further, defocus and astigmatism induce a larger wavefront error than higher-order aberrations in the human eye.[5,12]

In the present work, our AO module contains a motorized Badal optometer to correct defocus and a liquid crystal (LC) device to correct vertical and oblique astigmatism. The system was tested on a model eye with different trial lenses to induce aberrations and an Air Force target (USAF 1950) was used as a model retina to test the system's diffraction-limited resolution performance, to quantify the contrast improvement and intensity improvement. For a fair comparison, we aimed at a comparison with a system without AO and a 1.2-mm beam ($1/e^2$), but we did not have the optics in stock to build such a system and compromised on a system with a 1.3-mm beam size ($1/e^2$) instead. Finally, both systems were tested on a human eye with known aberrations. Speckle analysis was performed on the results to quantify the difference in the performance of the two systems.

2 Materials and Methods

For the model eye, the concept uses an image-based optimization algorithm with OCT B-scans for feedback to the AO

Table 1 Comparison of the proposed system with conventional OCT system and AO-OCT systems.

Parameter	Conventional OCT	AO-OCT	Present system with astigmatism and defocus correction
Beam size ($1/e^2$)	1.2 mm	6.0 mm	2.8 mm
Lateral resolution, estimated (FWHM)	23.3 μm	4.6 μm	10 μm
Practical imaging depth	Larger than thickness of retina	Less than half of retina[11]	Larger than thickness of retina[8]
Rayleigh lengths	269.5 μm	10.8 μm	49.7 μm
Isoplanatic patch	30 deg × 30 deg (estimated)	1.5 deg × 1.5 deg[9]	10 deg × 10 deg[8]
AO module	—	SH wavefront sensor and DMs	Badal optometer and LC device
Number of Zernike orders to be corrected		~5 orders	~2 orders (defocus and astigmatism)

module instead of a wavefront sensor. For human eye imaging, the prescription determined by a licensed optometrist was used for correction. Here, we will discuss the individual components of the setup.

2.1 *Motorized Badal Optometer*

Optometers are used for measuring the refractive errors of the eye.[28] Where the myopic or hyperopic eye cannot see an object clearly, optometers compensate defocus by introducing a conjugate wavefront to the aberrant eye, thereby removing aberrations and improving vision. A schematic of a Badal optometer is shown in Fig. 1.

The theoretical defocus introduced by the optometer is[28]

$$V = \frac{-\phi^2 \Delta Z}{1 - \phi \Delta Z (1 - \phi d)}, \tag{1}$$

where $\phi = \frac{1}{f_5}$ is the power of the L5 lens, ΔZ is the separation between the focal points f4 and f5, and d is the fixed distance between the eye and the lens. When the optometer satisfies the condition $d = f5$, and when the distance between the eye (E) and L5 is constant, this type of optometer is called a Badal optometer. The defocus generation formula for the Badal optometer is

$$V = -\phi^2 \Delta Z. \tag{2}$$

Defocus is linearly dependent on the distance ΔZ and can be controlled by changing the position of the lens L4. In the present work, we mounted lens L4 on a motorized stage and controlled it with the help of a program developed in LabVIEW. This motorized Badal optometer can generate a defocus ranging from −4.3 D to +4.3 D. By adjusting the reference arm length and the distance between the subject's eye and fixed ophthalmic lens (30 D, Volk Optical Inc., Mentor, Ohio), the galvanometer raster scanning mirror was conjugated with the eye's pupil. Since the pupil was not artificially dilated and the images were not vignetted, pupil wander was kept to a practical minimum.

2.2 *Liquid Crystal Module*

Hashimoto[29] and Tanabe et al.[30,31] showed the potential of LC devices for dynamic compensation of optical aberrations. In the present work, we used a transmissive LC device fabricated by Citizen Technology Center Co., Ltd., to correct for astigmatism.[31] This LC module consists of four LC cells (A, B, C, D). Cells A and C were used for oblique astigmatism correction. As these devices are sensitive to the polarization state of the light, one cell was used to correct the horizontal polarization state, while the other corrected the vertical polarization state of the beam. Similarly, cells B and D were used for vertical astigmatism correction. The dimensions of the LC device are 9 mm × 30 mm × 38 mm (length × width × height). The optical loss of the four LC cells was ∼38% at 840 nm, quantified with an Ophir broadband power meter. The thickness of the cell is 0.6 mm, and its flatness is $\sim\lambda/10$. Its aperture size is about 4.0 mm, and it can be operated in temperatures ranging from −20°C to 75°C.[29] Each of these LC cells was connected with a transparent electrode, to supply a specific driving voltage to each cell. These driving voltages are rectangular waveforms without an offset at 1-kHz frequency, and the magnitude of the waveform is proportional to the induced astigmatism. The required operating voltages for the LCs ranged between 1.5 V_{rms} (root mean square) and 2.5 V_{rms}, which is less than 5 V, meaning that it can be run by the power supply of a personal computer without the need for an expensive high-voltage amplifier.

2.3 *Optimization Algorithm*

In passive-auto-focusing technology, image quality parameters such as sharpness or contrast are used to optimize focusing instead of an external light source and sensor for distance measurements.[32] Liu et al.[33] and Sun et al.[34] discussed several optimization algorithms and metrics for autofocusing. The present work is based on passive autofocusing technology, and we have coined it "image-based optimization." We used two separate aberration-correction modules that both performed relatively slowly compared with high-speed DMs. We centered our approach on a sequential/coordinate search with a hill climbing algorithm.[17–19,21,22,35–37] While this algorithm is not likely to perform as well and as efficiently as AO-dedicated algorithms such as the DONE algorithm,[25] the hill-climbing algorithm is easily implemented and can provide decent correction within a few iterations.[36] We combined the hill-climbing algorithm with a merit function that used the normalized variance (NV) of a B-scan as an image-quality-judgment metric. These NV values were fit with a Gaussian to determine the optimum correction. The NV of a B-scan can be defined as

$$\mathrm{NV} = \frac{\mathrm{Variance(grayscale\ values\ in\ the\ B\text{-}scan)}}{\mathrm{Mean(grayscale\ values\ in\ the\ B\text{-}scan)}}. \tag{3}$$

The NV of a B-scan is resistive to noise fluctuations and generates a negligible number of local maximums, thereby avoiding the convergence to local maximums; it improves the convergence accuracy and speed of convergence.[33,34]

Since the aberrations are treated here as independent Zernike modes, the correction was done in a sequential manner. In the initial step of aberration correction, defocus was corrected by using the OCT B-scan images for feedback and optimization, followed by vertical and oblique astigmatism correction.

2.4 *Experimental Setup*

The experimental setup used in this work is shown in Fig. 2, where LS is a broadband light source (super luminescent diode SLD-371 from Superlum), with a central wavelength of 840 nm and an optical bandwidth of 51.5 nm [full width at

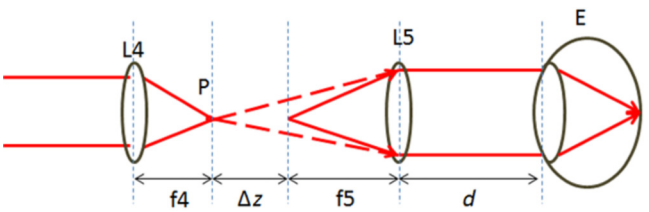

Fig. 1 Badal optometer, where p is the position of the focus, f5 is the focal length of fixed lens, d is the distance between the subject and the fixed lens. E is the eye. Defocus is induced by moving the lens L4.

half maximum (FWHM)], which can give a theoretical axial resolution of about 6.1 μm (in the air with $n = 1$).

2.5 *Measurement Procedure on Humans*

A protocol for measurements on human subjects was approved by the Institutional Review Board of Utsunomiya University, and it adhered to the tenets of the declaration of Helsinki. Measurements were performed on one human subject. The eyes of the subject were not dilated. The power of the light incident on the eye was at all times lower than 600 μW, a power that is considered safe according to the safety standards up to a time period of 8 h or more.

3 Results

3.1 *Calibration of the Wavefront Aberration Correctors*

To generate conjugate defocus and astigmatism values, we need to know the aberrations that can be compensated with the Badal optometer and the LC device. The Badal optometer and LC device were calibrated with the help of an SH wavefront sensor (WFS150-5C, Thorlabs). For calibration, the SH wavefront sensor was mounted in the sample arm in close proximity to the ophthalmic lens (L5) (see setup in Fig. 2). The dual-axis single mirror galvanometer scanner was kept stationary. When the Badal optometer was calibrated, the LC device was not used and vice versa.

By changing the position of lens (L4) (see setup in Fig. 2), we measured the defocus values with help of the SH wavefront sensor. The traveling length of the translation stage is about 12 mm, and at 6 mm the defocus was set to 0 D. The measured defocus values were plotted as a function of lens position, as shown in Fig. 3. The compensation range of the Badal optometer was −4.3 D to +4.3 D. One can enhance this range by choosing a translation stage with a wider range. Similarly, the compensation range of the LC device for vertical astigmatism and oblique astigmatism was tested with various voltages (Fig. 4).

Figures 4(a) and 4(b) show the graphs of vertical and oblique astigmatism values generated by the LC device as a function of the V_{rms} voltage, respectively. The LC can generate −2.5 D to +2.5 D of correction for both the vertical and oblique astigmatism channels. These values were later used to optimize correction of astigmatism in sensorless mode and when the instrument was used on a human subject with a prescription.

The time response of the LC device was measured with the SH wavefront sensor as well, and it took more than 20 s to achieve a stable correction for a correction of 2 D (Fig. 5).

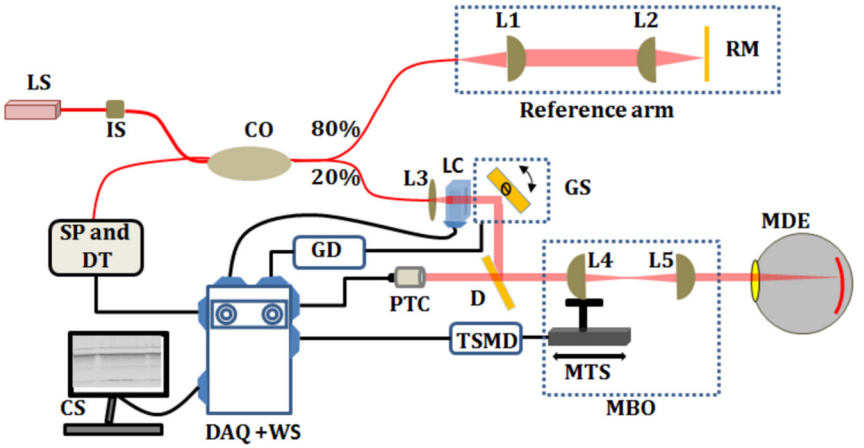

Fig. 2 Schematic of the developed OCT system with a 2.8-mm beam and defocus and astigmatism correction. The light source (LS) is connected to an optical isolator (AC Photonics), which prevents damage to the source by backreflection from the interferometer. After passing the isolator (IS), the light was fed into an 80:20 coupler (CO, Gould Fiber Optics). 80% of the light was directed to the reference arm, and 20% was directed to the sample arm. The reference arm consisted of a 25-mm (L1) focal length lens for collimation and a 25-mm (L2) lens to focus the beam on the reference mirror (RM). The sample arm consisted of a collimator lens with a focal length of 13.86 mm (L3). The collimated beam was fed into the LC device (LC, Citizen Holdings), which was driven by four driving waves generated with two NI PCIe-6353 input-output (IO) boards, each connected to a BNC-2110 breakout box (both National Instruments). The output beam from the LC was raster scanned by the dual axis single mirror galvanometer scanner (GS, T.E.M. Japan), operated through LabVIEW. The output beam from the galvanometer scanner was directed toward the dichroic mirror (D). From there, the light was reflected toward the Badal optometer, which comprises a lens (L4) with focal length 30 mm mounted on a motorized translation stage and a fixed lens (L5) with 30 D optical power (Volk Optical Inc., Mentor, Ohio). The pupil-tracking camera (PTC) was used to position the beam onto the sample. The backreflected light from the sample and reference arm combined at the coupler and generated an interference signal. This signal was spectrally dispersed by the grating in the spectrometer and detected with the line-scan camera (Basler SPL2048). The detected signal was grabbed with a frame grabber (NI PCIe-1433, National Instruments). When the aberration correction module was switched on, the LabVIEW program controlled the motorized linear translation stage (Z812B-MT1/M-Z8, Thorlabs) through a translation stage motor driver (TSMD). Defocus was introduced by changing the position of lens L4. The image-based optimization algorithm searched for the highest NV values. After correcting defocus, the LC was used to correct vertical and oblique astigmatisms.

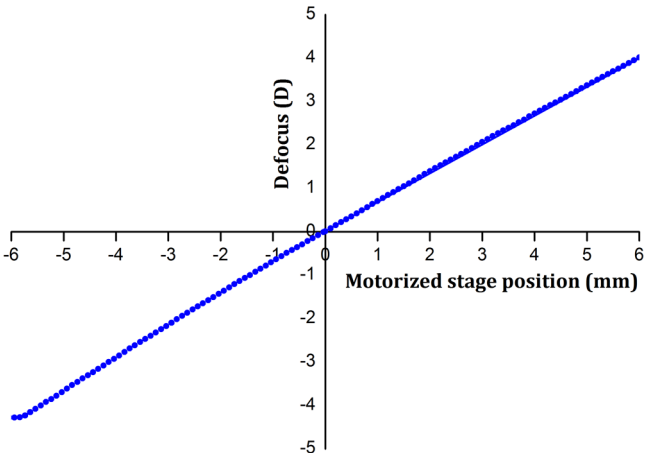

Fig. 3 The induced defocus as a function of the position of the Badal lens in the Badal optometer. The Badal lens position is shown on the horizontal axis, and the vertical axis shows the defocus values. The Badal optometer covered a defocus range from −4.3 D to +4.3 D.

3.2 *Resolution and Contrast Improvement Quantification*

The diffraction-limited performance of the imaging system was tested with a US Air Force resolution test chart. In the sample arm, we introduced −1 D of defocus and +1 D of vertical astigmatism and −1 D of oblique astigmatism. These aberrations were corrected automatically with the sensorless correction, maximizing the NV value. It took 1 min 9 s to finish the aberration correction, but since the amount of correction per step was smaller than the correction shown in Fig. 5, it was not necessary to wait for 20 s for each astigmatism correction step.

Figure 6 shows the *en face* images generated before and after correction of each aberration correction. These *en-face* images were generated by summing the backreflected intensity data. The theoretical diffraction-limited lateral resolution of the present system is 10 μm. At this resolution, the fifth group fifth element of the Air Force target should be resolvable.

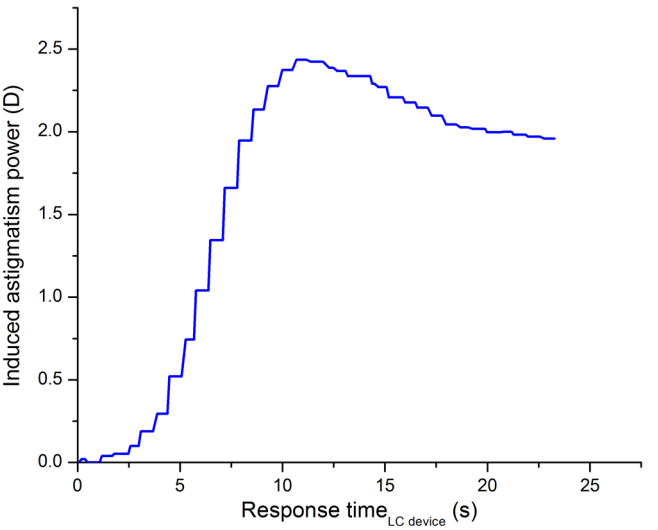

Fig. 5 The induced astigmatism power as a function of LC device response time. Most of the correction is achieved over the first 10 s, but it took more than 20 s to achieve a stable correction.

After correction of every aberration, the lateral resolution of the system increases and ultimately reaches the diffraction-limited resolution (Fig. 7). Figure 7(b) shows the intensity profile of the fifth group fifth element of a USAF resolution test target data that is segmented along the vertical direction marked with a red color line in Fig. 7(a) and normalized with their corresponding mean value.

In an ideal system, when the diffraction-limited resolution condition is met, the intensity profile across these line bars should generate a square wave shape. In Fig. 7(b), one can observe that these lines are difficult to resolve before correction, but after aberration correction these lines are easily resolvable, demonstrating a near-diffraction-limited performance.

The intensity improvement and contrast improvement before and after aberration correction were quantified for different spatial frequencies, using the resolution test chart. Measurements were plotted in Fig. 8. In these plots, the maximum intensity

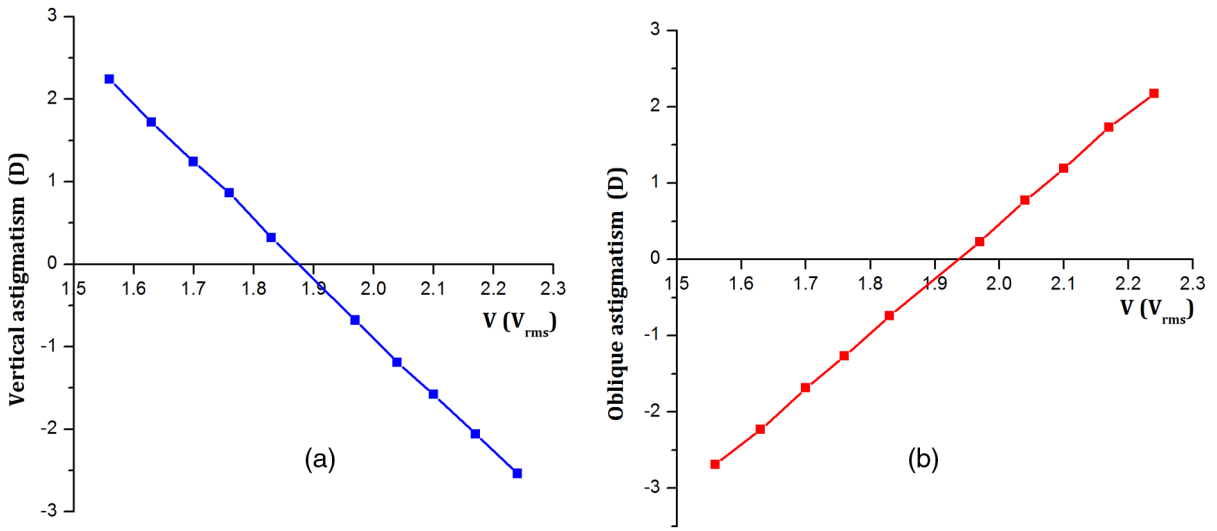

Fig. 4 (a) Vertical astigmatism and (b) oblique astigmatism measured with an SH wavefront sensor as a function of input voltage. The LC device could generate vertical astigmatism ranging from −2.5 D to +2.5 D and an oblique astigmatism ranging from −2.5 D to +2.5 D.

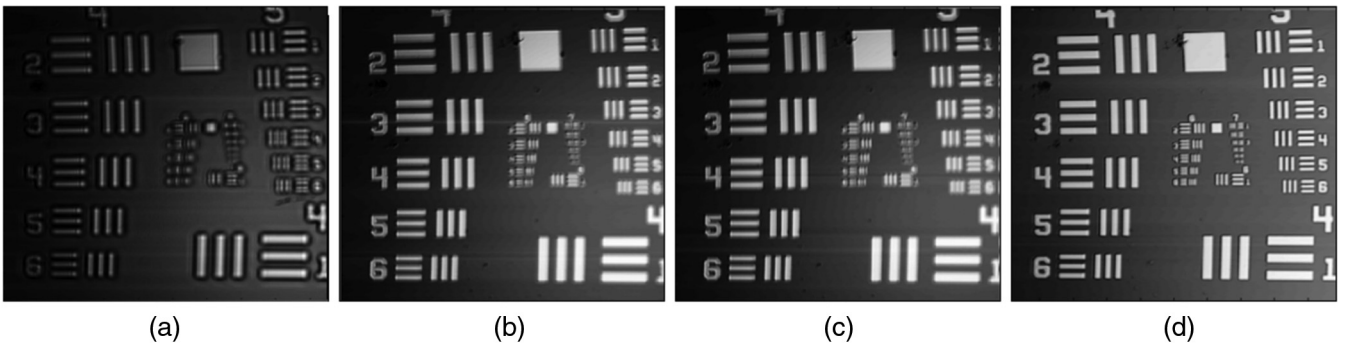

Fig. 6 (a) *En-face* image of the Air Force target before aberration correction. (b) The same image after defocus correction, (c) after vertical astigmatism correction, and (d) after oblique astigmatism correction.

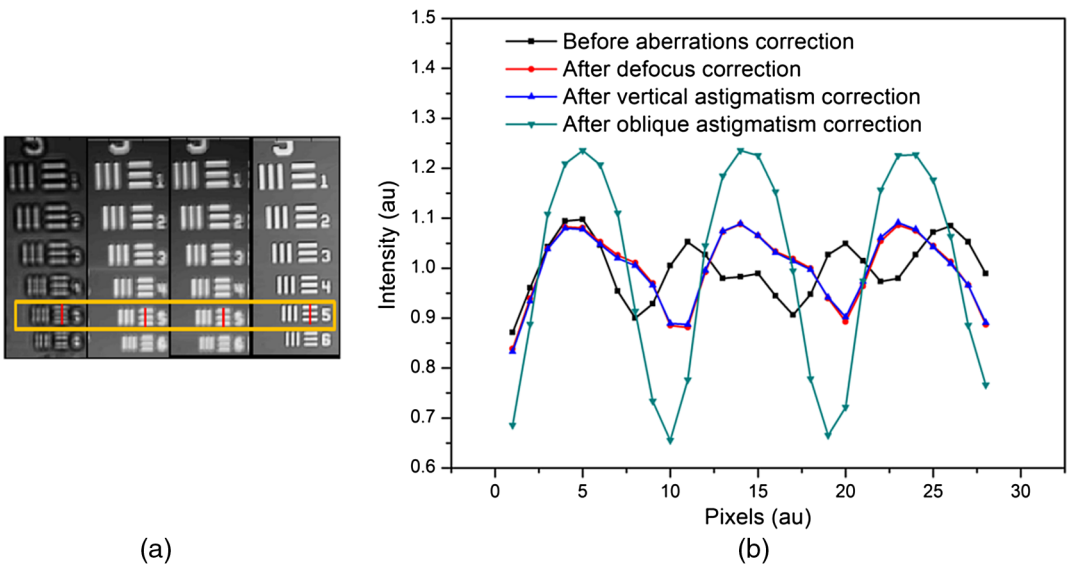

Fig. 7 (a) *En-face* image of the Air Force target's fifth group fifth element profile before aberration correction, after defocus correction, after vertical astigmatism correction, and after oblique astigmatism correction. (b) Intensity profiles across the fifth group fifth element before aberration correction, after defocus correction, after vertical astigmatism correction, and after oblique astigmatism correction.

across the fifth group first element to fifth group fifth element [these elements were shown in Figs. 6(a) and 6(d)] are plotted in Fig. 8(a). In Fig. 8(a), the vertical axis represents the maximum intensity (in arbitrary units) and the horizontal axis represents the spatial frequency in terms line pairs per mm (lp/mm), similar to Fig. 8(b). At the cut-off (diffraction-limited) resolution/spatial frequency after aberration correction, the maximum intensity improvement is 1.78 times. This shows that the intensity is good after the aberration correction, which helps to generate brighter OCT images. In Fig. 8(b), the vertical axis represents the contrast, and the horizontal axis represents the spatial frequency in terms line pairs per mm (lp/mm). At the cut-off (diffraction-limited) resolution, the contrast after final aberration is higher than the contrast before aberration correction. This is marked in the figure with a pink color arrow mark. The contrast values at a cut-off resolution of 10 μm or 50.2 line pairs per mm (lp/mm) are 0.05 before correction and 0.33 after correction, resulting in a contrast improvement of 6.9 times. This demonstrates that the visibility is better after the aberration correction, which helps to distinguish small features in OCT images.

3.3 *Dynamic Range Quantification*

A model eye with a defocus of −1 D was used for quantification of the dynamic range. A thin black paper sheet, supported by a flat aluminum plate, was used at the position of the retina in the model eye. B-scan images of the model eye with the 1.3-mm beam and 2.8-mm beam diameter systems are presented in Fig. 9, which shows the results before and after correction of relevant aberrations. The measured SNR gain that is achieved with the 2.8-mm beam diameter system compared with the 1.3-mm beam diameter system is 3.7 dB.

3.4 *Human Eye Imaging*

The present system is equipped for sensorless correction, but due to the slow response time of the LC device (Fig. 5), the correction time is too long for the imaging of human subjects. Even if the subject has a good fixation and does not blink often, the quality of the retinal images can drop significantly over 1 min, which can affect the NV in the images. However, the 2.8-mm system can also be used without sensorless operation

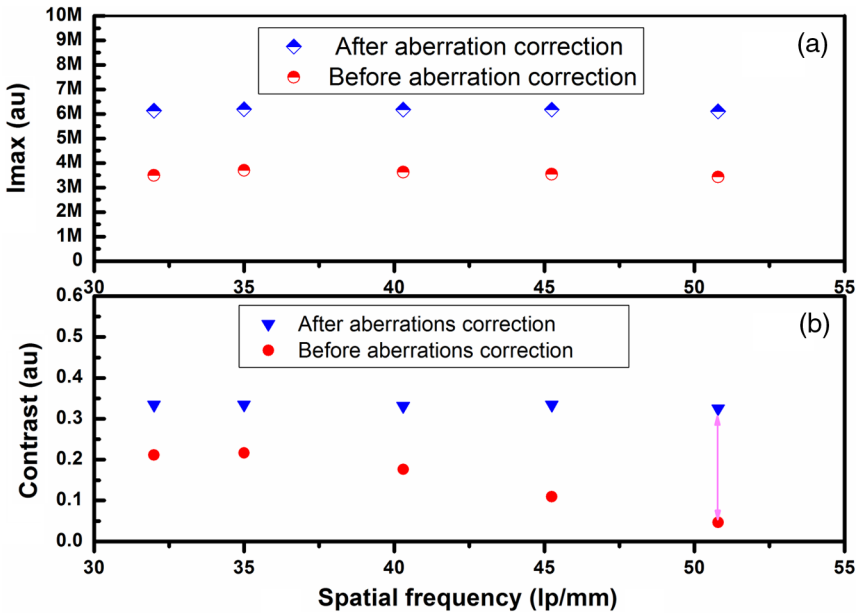

Fig. 8 (a) Maximum intensity across the spatial frequencies for before and after aberration correction. The vertical axis represents the maximum intensity (in arbitrary units) and horizontal axis represents the spatial frequency in terms line pair per mm. (b) Contrast across the different spatial frequencies before and after final aberration correction. The vertical axis represents the contrast (in arbitrary units), and the horizontal axis represents the spatial frequency in terms line pair per mm. The pink color arrow line marks the cut-off resolution to show the separation of contrasts before and after correction of aberrations.

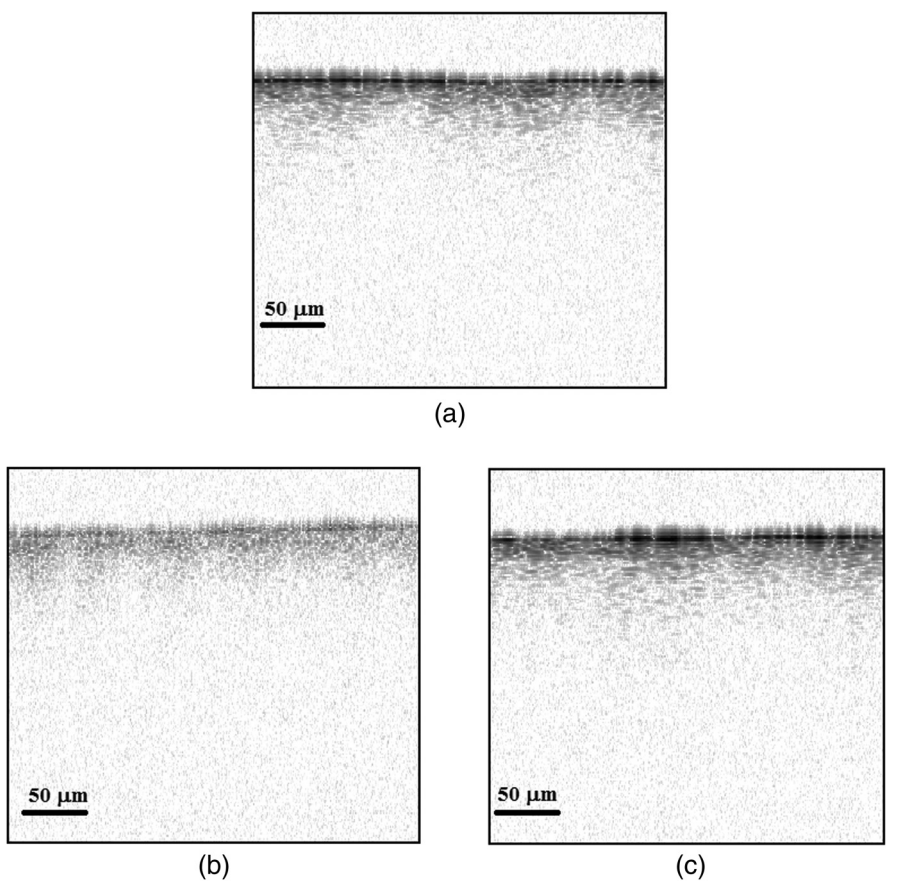

Fig. 9 (a) B-scan image of the model eye taken with 1.3-mm beam diameter OCT system (SNR = 48.6 dB). B-scan image of the model eye taken with the 2.8-mm beam diameter system (b) before aberration correction and (c) after aberrations correction (SNR = 52.3 dB).

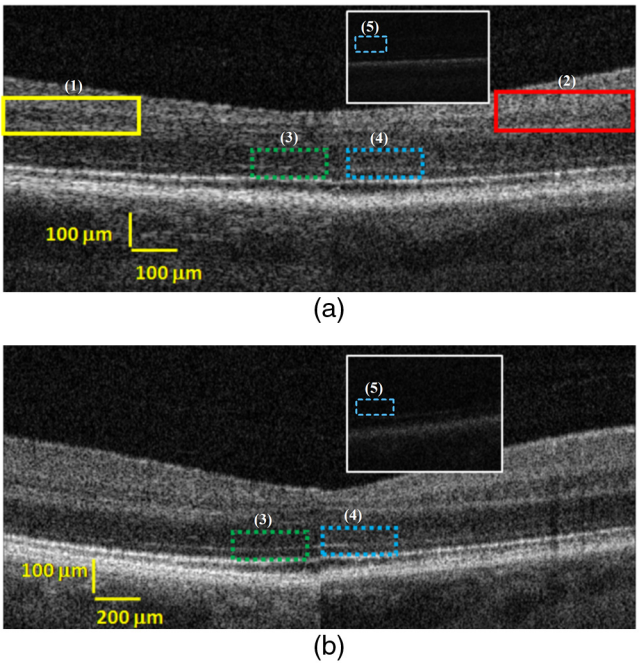

Fig. 10 B-scan images of the human retina. The left side of each image was taken with a standard OCT system with a 1.3-mm beam diameter, and the right side image was taken with the new system and a 2.8-mm beam diameter after correction of the aberrations (the inserts show images before aberration correction with the 2.8-mm system). Half of the image of 5-deg-wide scans (a) and 10-deg-wide scans (b) are shown. In (a), the yellow (1) and red (2) color highlighted areas are used for speckle analysis, to determine the width of the speckle pattern Moreover, areas enclosed by dotted boxes [1.3-mm beam diameter, green (3); 2.8-mm system, blue (4,5)] were used for quantification of the retinal layer intensities. More light seems to return from some of the nuclear layers, in comparison to the images taken with the 1.3-mm system. This may be due to collecting light over a larger angle.

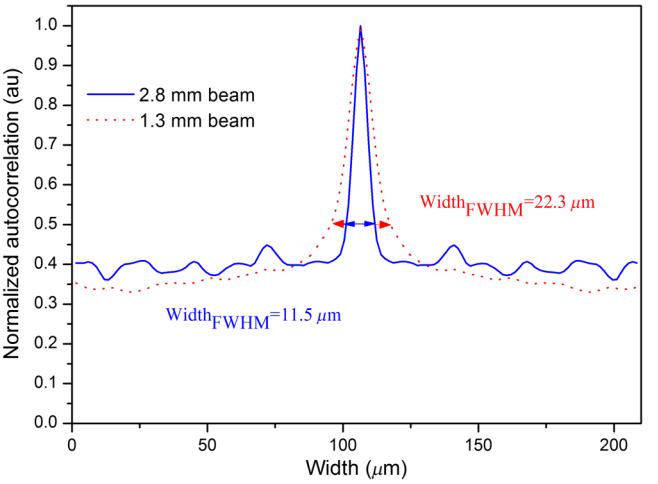

Fig. 11 The autocorrelation plot of the 1.3-mm beam diameter OCT system with an FWHM speckle width of 22.3 μm and the plot of the 2.8-mm beam diameter system after aberration correction with an FWHM speckle width of 11.5 μm.

if the refractive error values of the human eye are known. Once we set these values in the system, the desired conjugate aberration values can be generated to compensate for aberrations. In this section, OCT images taken with the 2.8-mm system of the human retina are compared with OCT images taken with the 1.3-mm beam diameter OCT system.

The right eye of the human subject was checked by a licensed optometrist, resulting in a prescription of −1.5 D defocus and −1.5 D cylinder (vertical astigmatism at 180 deg). The retina was imaged with a conventional system with a 1.3-mm beam diameter ($1/e^2$) with defocus correction and the new system with a 2.8-mm beam ($1/e^2$). Here, the prescribed defocus and vertical astigmatism values were converted using data from Figs. 3 and 4. The lens position and liquid crystal lens voltage values were set with the help of the LabVIEW program. In Fig. 10, aberration-corrected B-scan images obtained over 5 deg (a) and 10 deg (b) are shown. The left sides of these images were generated with the 1.3-mm beam diameter, while the right sides were made with a 2.8-mm beam diameter. The inserts on the right show the 2.8-mm beam diameter B-scan images before aberration correction. Due to the prescription of this subject, the images are faint without correction. Since speckle analysis requires a signal that is well above the noise floor for autocorrelation,[38] speckle analysis was only performed on the B-scan images of the human eye taken after correction with the new 2.8-mm system and a conventional 1.3-mm beam diameter OCT system. The areas that were used for comparison are highlighted with yellow (1) and red color (2) boxes [Fig. 10(a)]. The speckle profiles are plotted in Fig. 11 and show an improvement in speckle width of approximately two times for the 2.8-mm system. Ten B-scans were analyzed to measure the mean speckle diameter and its standard deviation. The average FWHM of the speckle diameter with the 1.3-mm beam diameter OCT system is 22.3 ± 4.3 μm. For the 2.8-mm beam diameter system, it is 11.5 ± 1.2 μm (Table 2).

The theoretical diffraction limited airy discs have a diameter of 21.6 μm (FWHM) for a 1.3-mm beam ($1/e^2$) and 10 μm (FWHM) for a 2.8-mm beam ($1/e^2$). The measured values are consistent with the theoretical values. The measured speckle sizes show that the speckle FWHM diameter with the presented system is ~2 times smaller than the 1.3-mm beam diameter system, giving a better image quality (Fig. 10).

The mean of the intensity occurring in the layers obtained with both the 1.3-mm and 2.8-mm systems was quantified and presented in Table 3. All B-scan images were generated with the same imaging parameters. The areas of interest are shown in Fig. 10 with dotted boxes colored green (3) for the 1.3-mm beam size system and blue (4, 5) for the 2.8-mm beam size system. Here, the maximum intensity would be represented by a value of 256, while the noise floor would be close to a value of 0. An overview of the measurements is given in Table 3.

These measurements confirm that the 2.8-mm system collects more photons from the sample, which results in a higher intensity than the intensity obtained with the 1.3-mm system.

Table 2 Theoretical and measured speckle diameters.

Pupil diameter (mm)	Theoretical speckle diameter (μm) (FWHM)	Measured speckle diameter (μm) (FWHM)
1.3	21.6	22.3 ± 4.3
2.8	10	11.5 ± 1.2

Table 3 Reflected intensity for different beam sizes and scanning widths.

Scanning angle (deg)	Mean intensity for 1.3-mm beam diameter system after correction (grayscale value)	Mean intensity for 2.8-mm beam diameter system before aberration correction (grayscale value)	Mean intensity for 2.8-mm beam diameter system after aberration correction (grayscale value)
5	50	11.2	62.5
10	48.8	10.1	59.9

4 Discussion

In comparison to a traditional AO-OCT system, a retinal imaging system with a 2.8-mm beam diameter requires a relatively low number of aberrations to be corrected. Here, we presented a system without a wavefront sensor and without a DM with a 2.8-mm beam size. Our system is less complex than a traditional AO-OCT design, and due to the small size of the LC device (9 mm × 30 mm × 38 mm), the concept can easily be implemented in commercial systems to achieve diffraction-limited resolution imaging. Since the LC response is slow (20 s for a single step in the correction of astigmatism), automatic aberration correction is not practical on a human subject. This problem can be overcome by measuring the refractive error of the human independently, prior to imaging. The refractive error is routinely measured independently in a clinical environment. Compensation can then easily be introduced with the system.

The LC device requires an operating voltage of less than 5 V, which can be supplied with a PC. DMs or multiactuator lenses[21] typically need high voltages that are generated with expensive high-voltage amplifiers. This system can correct defocus with a power ranging from −4.3 D to +4.3 D and vertical and oblique astigmatism with a power in a range from −2.5 D to +2.5 D. If one wants to correct aberration with higher speed and a larger range, or correct a larger number of orders, for instance for a system with a larger beam size, a deformable-mirror,[19] a multiactuator adaptive lens,[21] or multiactuator adaptive lens and variable focal lengh[22]-based sensorless AO-OCT concept may be a better option. The used defocus correction module is a motorized Badal optometer, which is driven through USB, whereas a liquid lens for defocus correction requires a high voltage driver and a graphics processing unit for depth-tracking optimization.[39] However, the liquid lens offers a higher correction speed, and because of its size it is easier to implement than a Badal optometer. In conventional AO-OCT experimentation, aberrations are determined with a wavefront sensor on (dilated) eyes in a relatively dark environment. In this experiment, a licensed optometrist performed the task of the wavefront sensor and determined astigmatism and defocus in a light-adapted eye that was not dilated. Since the optometrist took measurements in a well-lit room, the eye's pupil size is likely to have been between 2 and 4 mm,[40] which is large enough to accurately quantify these aberrations.[5] During measurements with the OCT instrument, however, which took place in a much darker room, the eye's pupil was probably larger than in the optometrist practice. If the beam was off-centered on this larger pupil, aberrations may have been incurred that were different from the aberrations that were measured by the optometrist. Since the 2.8-mm imaging beam was carefully centered without vignetting on the subject's undilated pupil, we are confident that defocus and astigmatism were corrected well. Using a 2.8-mm beam diameter, higher-order aberrations are expected to have had little influence as they tend to be small compared with defocus and astigmatism.[5,41]

If the correction speed of the LC device can be addressed, the current approach will be economically interesting as the concept is much cheaper than deformable-mirror-based systems. The system is compact, can cover a range of defocus and astigmatism that is practical in a clinical setting and can easily be implemented in current designs of commercial OCT systems as the LC device can easily be inserted directly behind the fiber collimator (see Fig. 2). Of course, this would also require motorization of the Badal optometer. The system was used for measurements over a width of 15 deg, which is an order of magnitude larger than typically used in conventional AO-OCT.

5 Conclusion

We presented an OCT system with a 2.8-mm beam diameter and a Badal optometer for defocus correction and an LC for vertical and oblique astigmatism correction. This system is less complex and can be made at a lower cost compared with traditional AO-OCT systems with a 6-mm beam. While the system does not achieve the same lateral resolution as provided by state-of-the-art AO-OCT systems, a lateral resolution of 11.5 μm can be achieved over a width of at least 15 deg by 15 deg, which is a factor of 10 larger than traditional AO-OCT systems. The system can correct the defocus ranging from −4.3 D to +4.3 D and vertical and oblique astigmatism ranging from −2.5 D to +2.5 D. We showed the performance of the system at the diffraction-limited resolution with the help of an Air Force target resolution test chart. A gain of 6.9 times in the contrast was measured after aberration correction at the cut-off spatial resolution. We also quantified an SNR gain of 3.7 dB compared with a conventional 1.3-mm beam diameter OCT system. Furthermore, we performed imaging on a human subject with both systems, showing more contrast in the less reflective layers of the retina. We also performed a speckle analysis, demonstrating a smaller speckle width compared with a conventional 1.3-mm beam diameter OCT system.

Disclosures

The authors do not have conflicts of interest, financial or otherwise.

Acknowledgments

Ministry of Education Culture, Sports, Science, and Technology-Govt. of Japan (scholarship Maddipatla Reddikumar).

References

1. D. Huang et al., "Optical coherence tomography," *Science* **254**(5035), 1178–1181 (1991).
2. R. Leitgeb, C. K. Hitzenberger, and A. F. Fercher, "Performance of Fourier domain vs. time domain optical coherence tomography," *Opt. Express* **11**(8), 889–894 (2003).
3. J. F. de Boer et al., "Improved signal-to-noise ratio in spectral-domain compared with time-domain optical coherence tomography," *Opt. Lett.* **28**(21), 2067 (2003).

4. A.N.S.I., *ANSI Z136 Safe Use of Lasers (2014)*, Laser Institute of America, Orlando, Florida (2014).
5. L. N. Thibos et al., "Statistical variation of aberration structure and image quality in a normal population of healthy eyes," *J. Opt. Soc. Am. A* **19**(12), 2329 (2002).
6. J. Porter et al., *Adaptive Optics for Vision Science: Principles, Practices, Design and Applications*, John Wiley & Sons, Hoboken, New Jersey (2006).
7. Y. Zhang et al., "High-speed volumetric imaging of cone photoreceptors with adaptive optics spectral-domain optical coherence tomography," *Opt. Express* **14**(10), 4380 (2006).
8. B. Cense and I. Isamuddin, "Adaptive optics for optical coherence tomography in retinal imaging: a reflection on past and future developments," *Rev. Laser Eng.* **41**(12), 1006–1011 (2013).
9. P. Bedggood et al., "Characteristics of the human isoplanatic patch and implications for adaptive optics retinal imaging," *J. Biomed. Opt.* **13**(2), 024008 (2008).
10. B. Cense et al., "Volumetric retinal imaging with ultrahigh-resolution spectral-domain optical coherence tomography and adaptive optics using two broadband light sources," *Opt. Express* **17**(5), 4095–4111 (2009).
11. O. P. Kocaoglu et al., "Imaging retinal nerve fiber bundles using optical coherence tomography with adaptive optics," *Vision Res.* **51**(16), 1835–1844 (2011).
12. H. R. G. W. Verstraete et al., "Feedforward operation of a lens setup for large defocus and astigmatism correction," *Proc. SPIE* **9896**, 98960T (2016).
13. M. Skorsetz, P. Artal, and J. M. Bueno, "Performance evaluation of a sensorless adaptive optics multiphoton microscope," *J. Microsc.* **261**(3), 249–258 (2016).
14. J. Antonello et al., "Semidefinite programming for model-based sensorless adaptive optics," *J. Opt. Soc. Am. A* **29**(11), 2428 (2012).
15. H. Hofer et al., "Wavefront sensorless adaptive optics ophthalmoscopy in the human eye," *Opt. Express* **19**(15), 14160–14171 (2011).
16. Y. N. Sulai and A. Dubra, "Non-common path aberration correction in an adaptive optics scanning ophthalmoscope," *Biomed. Opt. Express* **5**(9), 3059–3073 (2014).
17. S. Bonora and R. J. Zawadzki, "Wavefront sensorless modal deformable mirror correction in adaptive optics: optical coherence tomography," *Opt. Lett.* **38**(22), 4801 (2013).
18. Y. Jian et al., "Wavefront sensorless adaptive optics optical coherence tomography for in vivo retinal imaging in mice," *Biomed. Opt. Express* **5**(2), 547 (2014).
19. H. R. G. W. Verstraete et al., "Towards model-based adaptive optics optical coherence tomography," *Opt. Express* **22**(26), 32406 (2014).
20. K. S. K. Wong et al., "In vivo imaging of human photoreceptor mosaic with wavefront sensorless adaptive optics optical coherence tomography," *Biomed. Opt. Express* **6**(2), 580–590 (2015).
21. S. Bonora et al., "Wavefront correction and high-resolution in vivo OCT imaging with an objective integrated multi-actuator adaptive lens," *Opt. Express* **23**(17), 21931–21941 (2015).
22. Y. Jian et al., "Lens-based wavefront sensorless adaptive optics swept source OCT," *Sci. Rep.* **6**, 27620 (2016).
23. M.-R. Nasiri-Avanaki et al., "Optical coherence tomography system optimization using simulated annealing algorithm," in *Proc. of the 11th WSEAS Int. Conf. on Mathematical Methods and Computational Techniques in Electrical Engineering*, pp. 669–674, World Scientific and Engineering Academy and Society (WSEAS), Athens, Greece (2009).
24. M. J. D. Powell, "The NEWUOA software for unconstrained optimization without derivatives," in *Large-Scale Nonlinear Optimization*, pp. 255–297, Springer US, New York (2006).
25. H. R. G. W. Verstraete et al., "Model-based sensor-less wavefront aberration correction in optical coherence tomography," *Opt. Lett.* **40**(24), 5722–5725 (2015).
26. R. N. Clark, *Clarkvision Photography: Resolution of the Human Eye*, ClarkVision.com, http://www.clarkvision.com/articles/human-eye/.
27. C. R. Nave, "Scale model of human eye," *HyperPhysics*, http://hyperphysics.phy-astr.gsu.edu/hbase/vision/eyescal.html.
28. J. Schwiegerling, *Field Guide to Visual and Ophthalmic Optics*, SPIE Press, Bellingham, Washington (2004).
29. N. Hashimoto, "Liquid crystal active optics and its applications," *Micromechatronics* **51**(196), 8–14 (2007).
30. A. Tanabe et al., "Correcting spherical aberrations in a biospecimen using a transmissive liquid crystal device in two-photon excitation laser scanning microscopy," *J. Biomed. Opt.* **20**(10), 101204 (2015).
31. A. Tanabe et al., "Transmissive liquid-crystal device correcting primary coma aberration and astigmatism in laser scanning microscopy," *Proc. SPIE* **9717**, 97171N (2016).
32. N. Kehtarnavaz and H.-J. Oh, "Development and real-time implementation of a rule-based auto-focus algorithm," *Real-Time Imaging* **9**(3), 197–203 (2003).
33. X. Y. Liu, W. H. Wang, and Y. Sun, "Dynamic evaluation of autofocusing for automated microscopic analysis of blood smear and pap smear," *J. Microsc.* **227**(1), 15–23 (2007).
34. Y. Sun, S. Duthaler, and B. J. Nelson, "Autofocusing in computer microscopy: Selecting the optimal focus algorithm," *Microsc. Res. Tech.* **65**(3), 139–149 (2004).
35. M. Booth, "Wave front sensor-less adaptive optics: a model-based approach using sphere packings," *Opt. Express* **14**(4), 1339 (2006).
36. A. J. Wright et al., "Exploration of the optimisation algorithms used in the implementation of adaptive optics in confocal and multiphoton microscopy," *Microsc. Res. Tech.* **67**(1), 36–44 (2005).
37. P. N. Marsh, D. Burns, and J. M. Girkin, "Practical implementation of adaptive optics in multiphoton microscopy," *Opt. Express* **11**(10), 1123–1130 (2003).
38. B. Cense et al., "Retinal imaging with polarization-sensitive optical coherence tomography and adaptive optics," *Opt. Express* **17**(24), 21634 (2009).
39. M. Cua et al., "Retinal optical coherence tomography at 1 μm with dynamic focus control and axial motion tracking," *J. Biomed. Opt.* **21**(2), 026007 (2016).
40. H. K. Walker, W. D. Hall, and J. W. Hurst, *Clinical Methods, the History, Physical, and Laboratory Examinations*, 3rd ed., Butterworth, Boston.
41. J. Francisco Castejón-Mochón et al., "Ocular wave-front aberration statistics in a normal young population," *Vision Res.* **42**(13), 1611–1617 (2002).

Maddipatla Reddikumar is working toward his PhD at the Center for Optical Research and Education, Utsunomiya University, Japan. In 2010, he received his MSc degree in physics from the University of Hyderabad, India. Subsequently, he worked as a research fellow at the Birla Institute of Technology-Mesra. His current research interests are in optical coherence tomography, adaptive optics systems, biomedical optics, and optical imaging techniques.

Barry Cense is an associate professor at the Center for Optical Research and Education, Utsunomiya University, Japan. He received his PhD from Twente University in 2005. He is the coauthor of 44 peer-reviewed publications and one book chapter. His research interests are in retinal imaging, polarization-sensitive optical coherence tomography, ultra-high resolution optical coherence tomography and adaptive optics.

Biographies for the other authors are not available.